

# Resolving Atomic-Scale Defects in Conjugated Polymers On-Surfaces

Benjamín Mallada,<sup>[a, b, c]</sup> Qifan Chen,<sup>[c]</sup> Taras Chutora,<sup>[a, e]</sup> Ana Sánchez-Grande,<sup>[d]</sup> Borja Cirera,<sup>[d]</sup> José Santos,<sup>[d]</sup> Nazario Martín,<sup>[d]</sup> David Ecija,<sup>[d]</sup> Pavel Jelínek,<sup>[a, c]</sup> and Bruno de la Torre<sup>\*,[a, c]</sup>

**Abstract:** Atomic scale defects significantly affect the mechanical, electronic, and optical properties of  $\pi$ -conjugated polymers. Here, isolated atomic-scale defects are deliberately introduced into a prototypical anthracene-ethynylene  $\pi$ -conjugated polymer, and its local density of states is carefully examined on the atomic scale to show how individual defects modify the inherent electronic and magnetic properties of this one-dimensional systems. Scanning tunneling and atomic force microscopy experiments, supplemented with density functional theory calculations, reveal the existence of a sharp

electronic resonance at the Fermi energy around certain defects, which is associated with the formation of a local magnetic moment accompanied by substantial mitigation of the mobility of charge carriers. While defects in traditionally synthesized polymers lead to arbitrary conformations, the presented results clearly reflect the preferential formation of low dimensional defects at specific polymer sites, which may introduce the possibility of engineering macroscopic defects in surface-synthesized conjugated polymers.

## Introduction

The synthesis of conjugated polymers aims to improve their beneficial properties, such as high charge carrier mobility, unique light absorption, and emission characteristics,<sup>[1]</sup> which is useful for different technological applications, including light-emitting devices, solar cells, organic field-effect transistors, photocatalysis, and biosensors.<sup>[2,3]</sup> As a result of their strong structure-to-property correlations, defects play a central role in the physical properties of conjugated polymers. For example, it has been observed that structural and chemical defects disturb electronic conjugation throughout the polymer structure by

reshaping the  $\pi$  electron lattice, resulting in: (i) potential confinement of electronic excitations on small subunits that act as chromophores and, (ii) significantly reduced electron mobility.<sup>[4–9]</sup> Although the role played by these defects has been extensively addressed by theory,<sup>[10–14]</sup> reported experimental data refer to statistical properties of the entire heterogeneous collection of defects generated in the polymerization process.<sup>[8,12,15–20]</sup>

Recently, on-surface synthesis<sup>[21–24]</sup> has emerged as a new synthetic protocol for designing nanomaterials with atomic precision and customized electronic properties. Taking advantage of the two-dimensional confinement of a surface, polymerization reactions can lead to the formation of unprecedented large polymers under ultra-high vacuum (UHV) conditions, not accessible in solution chemistry. Particular attention has been paid to  $\pi$ -conjugated materials,<sup>[25]</sup> illustrated by the bottom-up synthesis of graphene nanoribbons.<sup>[24,26]</sup> Lately, the approach has shown the potential to design well-defined  $\pi$ -conjugated materials with exotic electronic properties, such as non-trivial band topology<sup>[27–30]</sup> or  $\pi$ -magnetism.<sup>[31]</sup> Furthermore, on-surface synthesis allows the characterization of these systems by combining surface science techniques such as scanning tunneling microscopy (STM) and high-resolution atomic force microscopy in a non-contact (nc-AFM) regime. This blend of techniques has the ability to resolve not only the topographic shape but the backbone of individual molecules<sup>[32]</sup> allowing the identification of the reaction products for each on-surface reaction step<sup>[33–35]</sup> together with their microscopic electronic structure via scanning tunneling spectroscopy (STS).

Such nanostructures are often subject to comprise atomic-scale defects arising from the synthesis process.<sup>[36,37]</sup> Importantly, defects can tailor intrinsic characteristics of the  $\pi$ -conjugated material by atomic rearrangement, resulting in stabilized open-shell configurations that feature nontrivial  $\pi$ -

[a] B. Mallada, Dr. T. Chutora, Dr. P. Jelínek, Dr. B. de la Torre  
Regional Centre of Advanced Technologies and Materials  
Czech Advanced Technology and Research Institute (CATRIN)  
Palacký University Olomouc  
78371 Olomouc (Czech Republic)  
E-mail: bruno.de@upol.cz

[b] B. Mallada  
Department of Physical Chemistry,  
Faculty of Science  
Palacký University  
78371 Olomouc (Czech Republic)

[c] B. Mallada, Q. Chen, Dr. P. Jelínek, Dr. B. de la Torre  
Institute of Physics,  
Academy of Sciences of the Czech Republic  
Prague (Czech Republic)

[d] Dr. A. Sánchez-Grande, Dr. B. Cirera, Dr. J. Santos, Prof. N. Martín, Dr. D. Ecija  
IMDEA Nanociencia, Ciudad Universitaria de Cantoblanco  
Madrid (Spain)

[e] Dr. T. Chutora  
Current address: Department of Physics, University of Alberta  
Edmonton, Alberta,  
T6G 2J1 (Canada)

Supporting information for this article is available on the WWW under  
<https://doi.org/10.1002/chem.202200944>

magnetism.<sup>[38–40]</sup> Even though defect engineering was a striking success story in inorganic semiconductors,<sup>[41,42]</sup> both for their mechanical and electronic properties, and also applied to organic hard materials, defect engineering has rarely been used in the design of soft matter so far. Thus, for further development of protocols for understanding and engineering defects in such structures, a detailed characterization of the electronic and geometric structure of low-dimensional defects in  $\pi$ -conjugated polymers is demanded.

In the following, we have deliberately introduced atomic-scale defects in on-surface synthesized polymers and deeply investigated their nature by using STM/STS, nc-AFM, and density functional theory (DFT). We study the prototypical anthracene-ethynylene  $\pi$ -conjugated polymer on Au(111) following our recently developed synthetic protocol.<sup>[29,43]</sup> Then, we induce formation of atomic-scale defects that can be harnessed to a given extent by increasing the annealing temperature during reaction processes. In particular, we identified statistically more abundant defects consisting of both atomic rearrangements and incorporation of atomic species and examined their impact on the electronic structure of the

polymer. Interestingly, we show that while some conformational defects hardly affect the intrinsic electronic structure of the polymer, certain atomically defined defect motifs can harbor localized spins at specific sites, which is revealed by the presence of a Kondo resonance<sup>[44,45]</sup> in the STS spectroscopy.

## Results

### Synthesis of defects-containing ethynylene-bridged anthracene polymers

The one-dimensional conjugated nanostructure, and its low-dimensional defects studied here, are synthesized directly on the Au(111) surface by thermal annealing after molecular deposition in ultra-high vacuum. Deposition of the molecular precursor 11,11,12,12-tetrabromoanthra-*p*-quinodimethane (hereafter 4BrAn, see the sketch in Figure 1a) on a clean Au(111) surface and subsequent annealing at 500 K for 30 minutes in UHV, results in the formation of a low-bandgap ( $\approx 1.5$  eV) ethynylene-bridged anthracene polymer (see Figure 1b, and ref.

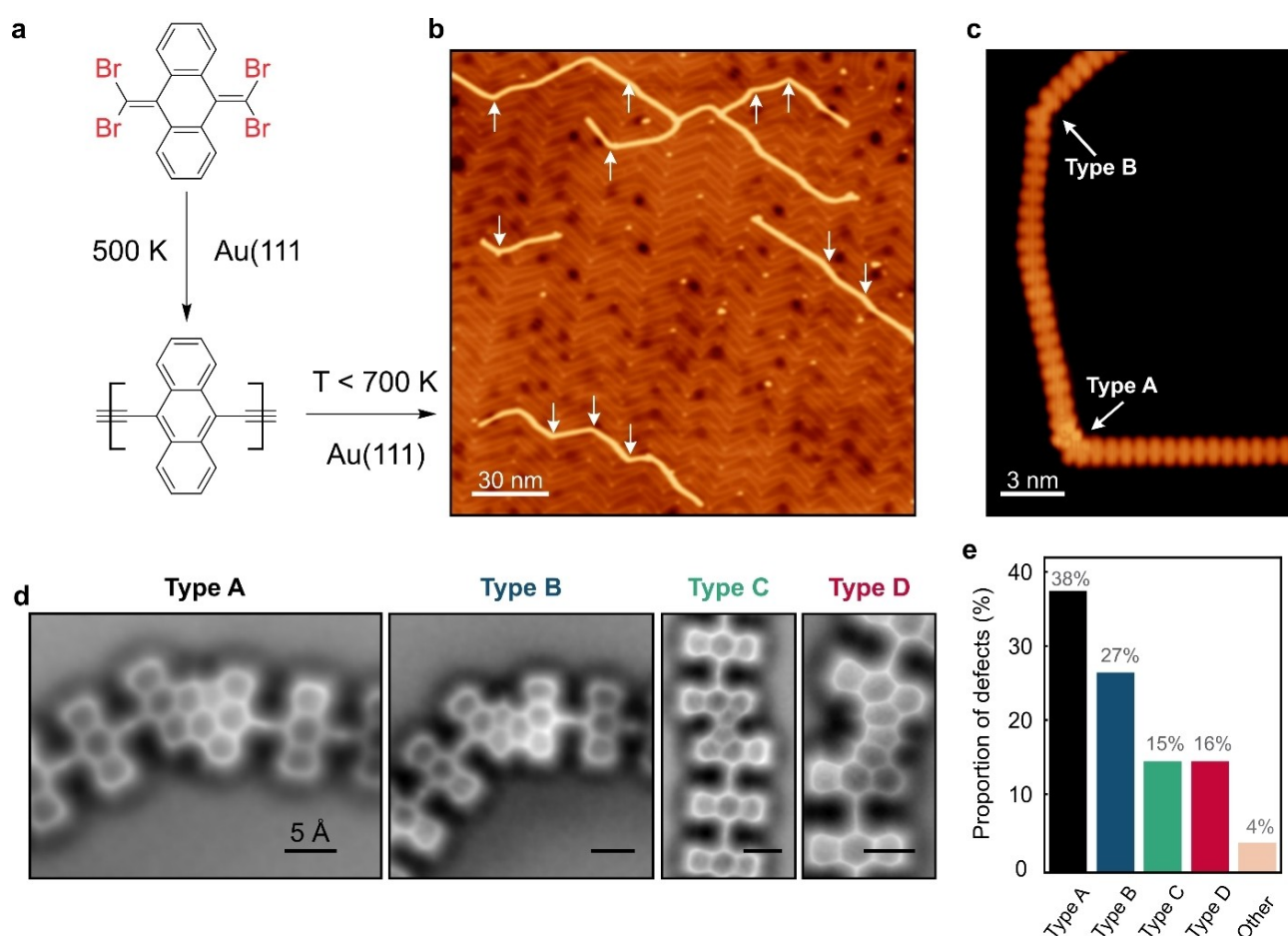


**Figure 1.** Low-dimensional structural defects in anthracene-ethynylene polymer on Au(111). a) Scheme of the reaction sequence of 4BrAn (11,11,12,12-tetrabromoanthra-*p*-quinodimethane) precursor after being deposited on Au(111) and annealed. b) Topographic overview ( $I_t = 5$  pA,  $V_{\text{bias}} = 200$  mV) of the polymer-decorated sample upon annealing below 700 K. c) Close-up topography of a polymer containing kinks ( $I_t = 10$  pA,  $V_{\text{bias}} = 5$  mV). d) nc-AFM (Laplacian filtered) elucidation and statistics of the most found low-dimensional defects. e) Histogram of relative abundance of defects (77 defects were counted in total).

[43] for a detailed characterization of its pristine properties). Defects in such polymers are rare and pristine polymeric segments up to hundreds of nanometers can be found routinely.

Subsequent annealing of the surface leads to distorted molecular wires with a much greater number of structural defects. Statistical analysis of the defect density at different temperatures produces a clear trend with annealing temperature (Figure S1). The number of intermolecular defects drastically increases upon annealing the sample at 500 K, indicating the onset of the defect formation. Further annealing up to 700 K gradually introduces intramolecular defects into the polymers. The overview and detailed STM topographies upon annealing <700 K, shown in Figures 1b, c, display the on-surface synthesized ethynylene-bridged anthracene wires as a result of successful polymerization. In addition, the molecular wires comprise in-plane (plane of the surface) joints between pristine ethynylene-bridged anthracene segments with a measurable angle mainly in a narrow range from 60° to 80°, which will be later identified as type A and B defects (marked by white arrows in Figures 1b, c). These defects are the majority over those that preserve the linearity of the polymer (type C, see below) and those featuring a small bending angle (type D, see below) as manifested in the statistical analysis (see Figure 1d, e). Recently, we reported that at the polymerization temperature ( $T > 500$  K), molecular vibrations are triggered both in the monomer unit and the linker,<sup>[46]</sup> inducing carbon rearrangements.<sup>[47]</sup> In such pristine ethynylene-bridged anthracene-polymers, the relative longitudinal stiffness of the ethynylene bridge promotes bending of the polymer over longitudinal reactions, while preserving the chemical structure of the monomer, unlike polymers with cumulene-like bridges.<sup>[46]</sup> Thus, the featured kinks in anthracene-ethynylene polymers can be rationalized by such structural bending in the linker moiety together with increased diffusion of the polymer on the surface at elevated temperatures, facilitating the backbone realignment. In addition, as we will explain below, for type A defect, it is necessary the incorporation of an extra single atom.

Post-annealing of the substrate to higher temperatures ( $T > 700$  K) results in a sample with predominantly lateral bonds between polymers due to the activation of the C–H bonds at the periphery of the monomers and the high lateral mobility of the species on the surface (see Figure S2) which largely increases the density of defects (Figure S1).

### Structural characterization

We attained structural characteristics of more prominent defects at the atomic level employing non-contact AFM measurements with a CO-functionalized tip<sup>[32]</sup> (Figure 1d and Figure S3). Statistic of defects observed in several experimental sessions, reveals that two distinct types of low-dimension structural defects (labeled A and B in Figure 1c,d) are the most frequently encountered in our experiments for all investigated annealing temperatures. Thus, below, we focus our discussion on a detailed comparison of polymers with type A and B defects

that are by far the most representative ( $\approx 38\%$  and  $\approx 27\%$  of the total number of defects, respectively). As illustrated by the high-resolution nc-AFM image (see Figure 1d), the type A defect consists of two hexagons and a single pentagon formed at the junction between two adjacent anthracene monomers instead of the ethynylene bridge found in pristine polymers. On the other hand, type B (see Figure 1d) consist of both six- and five-membered rings at the junction.

Type B defect can be rationalized by a bare frustrated transformation reaction from ethynylene- towards pentalene-bridged polymer, whereas the incorporation of an additional atom to the polymeric linker is required to account for the formation of defect type A. nc-AFM images allow to identify heteroatoms in the chemical structure due to their distinct van der Waals radii, bonding geometry, electron density, and substrate interaction.<sup>[48]</sup> Our nc-AFM images lead to atomic features with rather similar contrast which points to the formation of such defects with only carbon atoms. Individual carbon atoms are common residues in surface chemistry experiments with organic compounds. In our case, the cleavage of  $\text{=CBr}_2$  at the ends of the polymer provides the system with a reservoir of residual. The growth of type A and B defects involves rearrangement of the carbon atoms and  $\pi$ -conjugation around the ethynylene-bridge along with final cyclodehydrogenation reactions.

### Electronic characterization

Next, we turn the attention to the effect of such low dimensional type A and B defects on the intrinsic electronic properties of the polymers. The addition of an extra carbon to the bridge (type A defect) leads to significant differences in charge distribution at the junction, in addition to the structural rearrangement described above. To give a clearer picture it is worth to comparatively discuss both defects. To probe the electronic properties of polymeric sections featuring type A or type B defects, we performed scanning tunneling point spectroscopy (STS) measurements and differential conductance ( $dI/dV$ ) mapping on both types of defects and adjacent pristine segments. These measurements directly probe the energy- and spatial dependence of the local density of states (LDOS) of each carbon nanostructure.

In agreement with our previous reports,<sup>[43]</sup> two frontier resonances at  $-0.6$  eV and  $0.8$  eV are distinguished in STS data collected in pristine polymeric segments (cf Figure 2a), which are close to the onset of valence (VB) and conduction (CB) bands respectively (see Ref. [42]). The  $dI/dV$  map of the VB has states over the bridges and notably on the voids adjacent to the links. The  $dI/dV$  map of the CB shows states located on the edges of the anthracene moieties.

As expected, the  $dI/dV$  maps acquired on the defects show significant differences when compared to pristine ones. For type A defect,  $dI/dV$  map at  $0.8$  eV (i.e. at the CB) exhibits that signal barely changes around the defect, with bright features localized at the outermost anthracene edges (cf Figure 2a). Contrary, the map at the VB shows dim contrast at the defect

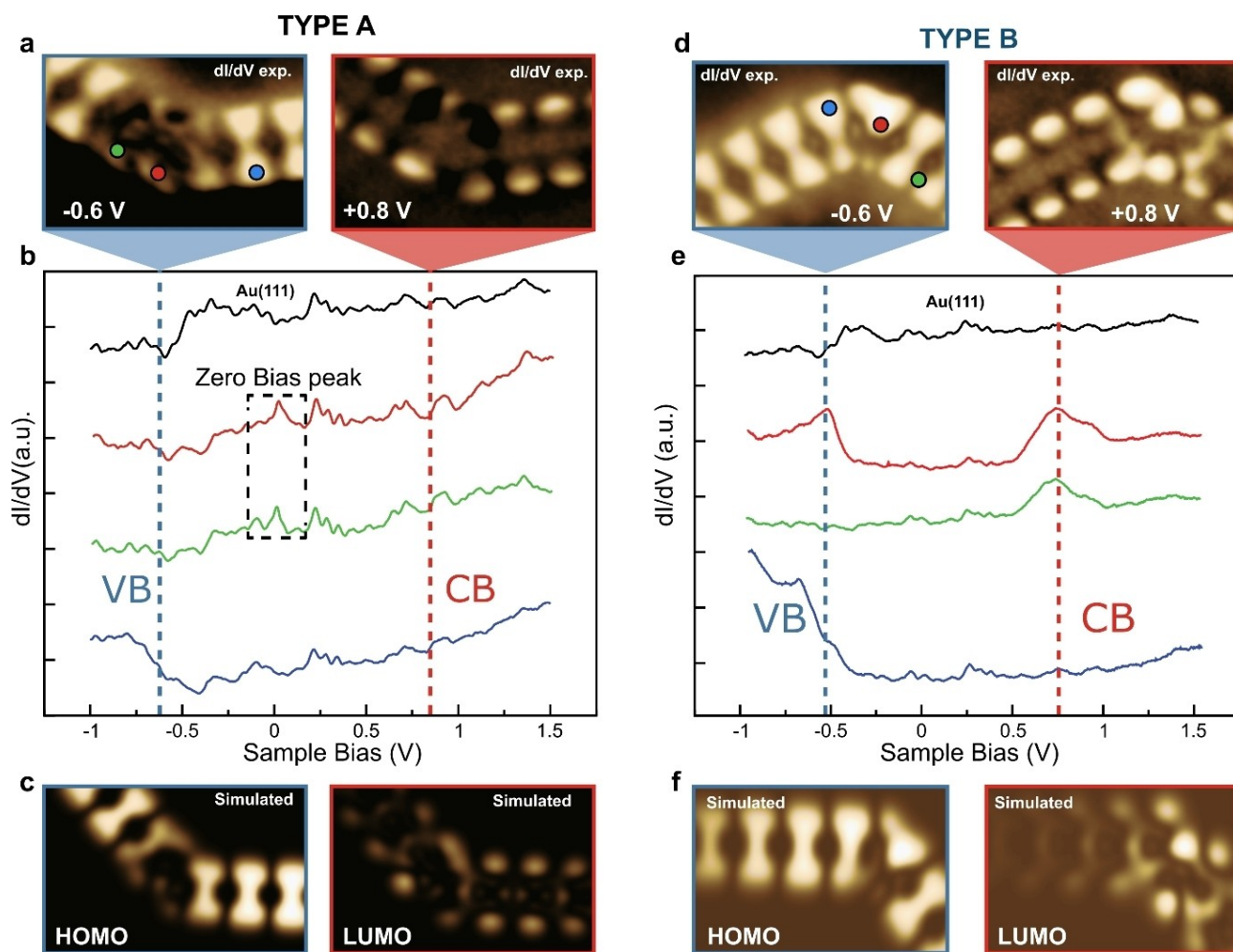


**Figure 2.** Conductance maps of type A and B defects. (a–d) Experimental  $dI/dV$  maps ( $V_{\text{mod}} = 20$  mV, 613 Hz) were acquired on the defect type A and B at two bias voltages ( $-0.6$  V and  $0.8$  V); (b–e) Experimental  $dI/dV$  spectra acquired on different sites of the defects type A and type B; (c–f) Calculated  $dI/dV$  maps for canonical DFT orbitals of HOMO and LUMO.

site and at the nearest anthracene units (Figure 2a,b), which may indicate a strong hybridization of the defect-induced electronic states with the polymer orbitals. The experimental findings are well supported by DFT-calculated  $dI/dV$  maps of a finite defective polymer (Figure 2c). However, for a detailed description, we have to look at the spin-polarized electronic states localized at the defect A and their corresponding energy alignment with the VB and CB of the polymer. Our DFT spin-polarized calculations of defect type A (see Figure S4) display both single-occupied (SO) and single-unoccupied (SU) states laying very close to the VB and CB respectively. Although this may affect the resolution of the VB and CB, our calculations mimic the important features, i.e. the lower contrast around defect for the VB and the high contrast at the features localized at the outermost anthracene edges for the CB.

On the other hand, spectra acquired at the junction of a type B defect exhibits resonances at both  $0.8$  eV and  $-0.6$  eV (Figure 2e), and the CB and VB maps of the junction display a substantial charge density at the defect site. Importantly,  $dI/dV$  maps of both VB and CB (cf Figure 2d) show that the spatial

distribution of the band structure is barely disturbed around the defect. The images display that the band structure is not affected by the presence of the defect, indicating a low impact of such defect on the electronic properties of the polymer, at least for the frontier orbitals. Again, the DFT-simulated  $dI/dV$  maps (cf Figure 2f) are in good agreement with the experimental data reproducing the aforementioned features.<sup>[37]</sup>

## Discussion

Thus, in the following, we will discuss the impact of both defects on the conjugation of the polymer. For such a purpose, we employ high-resolution nc-AFM imaging with a CO-tip that has demonstrated the ability to resolve not only the chemical structure of individual molecules but also the bonding character. As discussed earlier, type A defect consists of two six-member and one five-member ring. Nc-AFM images of the defect clearly resolve a bright spot in the center of the linker in neighboring monomers (Figure 3a–c), which has been ascribed



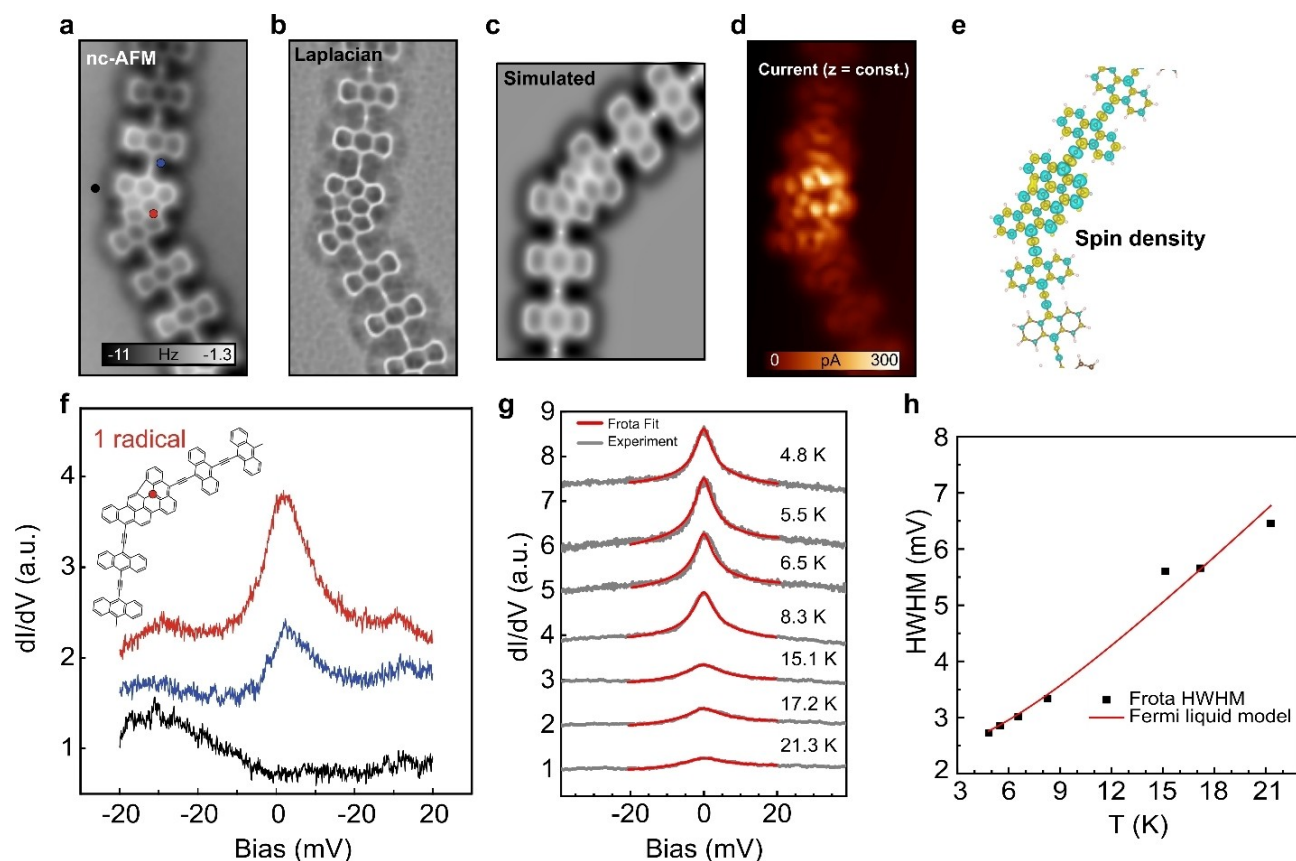


**Figure 3.** Structural characterization of type A defect. a) Constant height nc-AFM with CO-tip imaging of the type A defect. b) Laplace filtered nc-AFM image. c) Simulated AFM image of the defect with the probe particle model. d) Spin density calculated by DFT. e) Spin density calculated by DFT. f) STS spectroscopy near Fermi level showing a Zero Bias Peak on the defect site. In the inset, conjugation of the anthracene-ethynylene polymer with type A defect. g) Temperature evolution of the Zero Bias Peak (gray line) fit with a Frota function (red line) obtained on the defect site. h) Half width at the half maximum (HWHM) values extracted from the Fano fit of the Zero Bias Peak as a function of the temperature. The Kondo temperature is extracted from the Fermi-liquid model:  $\Gamma = \frac{1}{2} \sqrt{(\alpha K_B T)^2 + (2K_B T_K)^2}$  with an empirical parameter of  $\alpha = 6.9 \pm 0.3$  and a Kondo temperature of  $T_K = 27 \pm 2$ .

to the large electron density of the triple bond, thus demonstrating the ethynylene character of such linkers. Meaningfully, in such a form of  $\pi$ -conjugation, the defect should harbor a single localized unpaired electron. In fact, STM constant height images at low bias voltage (0.005 V) show brighter contrast around type A defects (Figure 3d) compared to the straight polymeric segment, reflecting enhancements of the local density of states (LDOS) near the Fermi level. Though these bright regions extend over the closest anthracene monomers and their junction as well, the brighter signal can be located in the anthracene closest to the pentagon moiety. Comparatively, such low-energy LDOS enhancements are absent in type B defects (see Figure 4d).

A better understanding of the origin of these LDOS differences in type A defects can be achieved by recording the spectroscopic differential conductance ( $dI/dV$ ) around Fermi level with the STM tip positioned at different sites above the defect. Spectra acquired on the type A defect reveals the presence of a sharp zero-bias peak (ZBP) (Figure 3f) located at the junction and adjacent anthracene monomers, rapidly vanishing into neighboring anthracene moieties. The shape of the ZBP is close to that of a Lorentzian with a line width of

approximately 3.5 mV. The narrow width of the ZBP rules out the direct association of this peak with a molecular resonance. The zero-bias features can be well fit with a Frota (see Figure 3g) or Fano (see Figure S5) functions<sup>[49,50]</sup> and thus are attributed to a Kondo resonance arising from the screening of magnetic moment (unpaired electron) by the conduction electrons residing in the Au(111), as already expected from the chemical resonance form of the defect. The relationship between the observed ZBP and the Kondo effect is further demonstrated by measurements of  $dI/dV$  spectra at different temperatures (Figure 3c). The width of the resonance line increases with temperature following the characteristic behavior of a weakly coupled Kondo system with a Kondo temperature  $T_K = 27 \pm 2$  K, and a multiplicative factor  $\alpha = 6.9 \pm 0.3$ , in line with a quenching of the ZBP with temperatures above 21 K (Figure 3g-h).<sup>[51,52]</sup> Remarkably, we found that also Fano function fits well our data leading a Kondo temperature of  $T_K = 38 \pm 2$  K (see Figure S5).

The existence of an unpaired spin density in the defect is corroborated by theoretical calculations of a free-standing polymeric section comprising one type A defect. Spin-polarized DFT reveals significant spin density at the defect site which

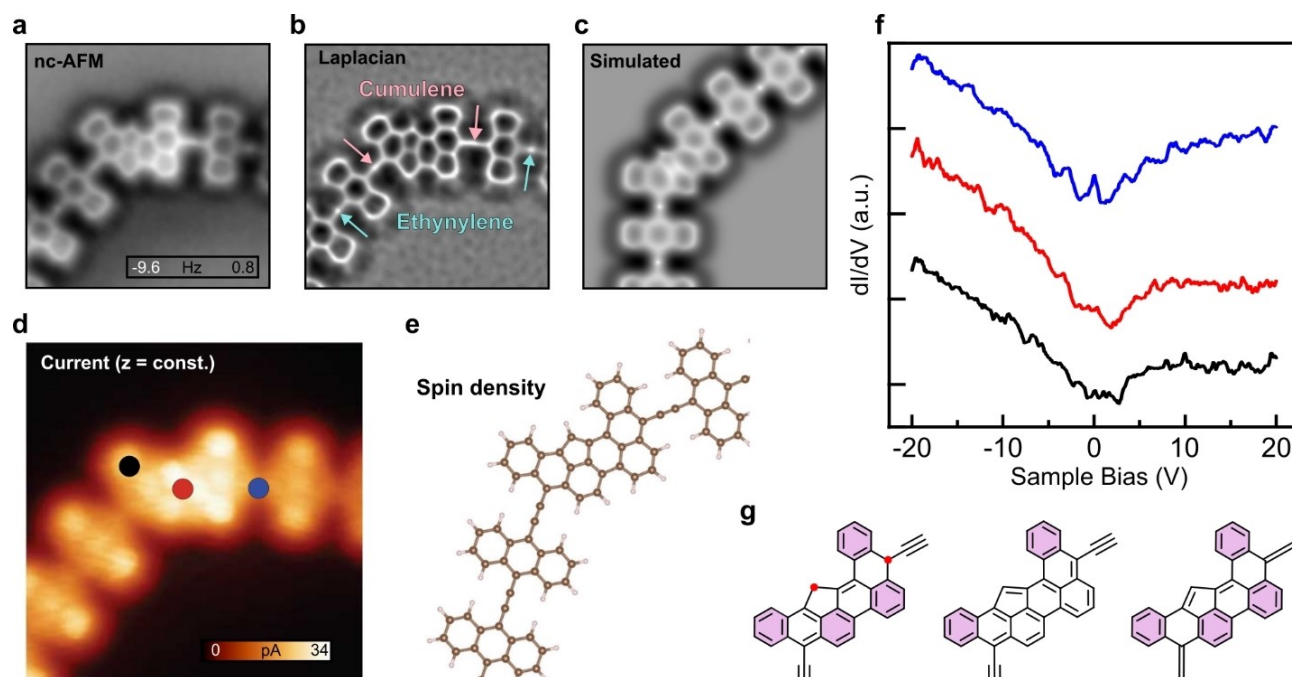


**Figure 4.** Structural characterization of type B defect. a–b) AFM Constant height current images with CO-functionalized tip of the type B defect. b) Laplace filtered nc-AFM image. c) Simulated AFM image with probe particle of the type B defect. d) High resolution constant height current image of the defect with the positions of the spectroscopies. e) Spin density calculated by DFT. f) STS spectroscopy near Fermi for selected regions (red, blue and black dots) of the defective polymer. g) Conjugation models for the type B defect with Clar's sextets highlighted: open-shell (left), close-shell ethynylene (center), and close-shell cumulene (right).

extends towards the monomers nearby (Figure 3e). Hence, the bright regions in STM images near Fermi energy are caused by the localization of a single magnetic moment around the defect site. According to our measurements, such polarized spin density survives on the Au(111) surface and gives rise to the ZBP due to the Kondo phenomenon, as previously encountered in other magnetic carbon-based nanomaterials.<sup>[38]</sup>

Next, an analysis of nc-AFM images of type B defect shows distinct characteristics from its type A counterpart. The formation of type B defect, which involves the constitution of six- and five-membered rings at the junction, can give rise to distinct resonance forms of the  $\pi$ -conjugation: (i) an open-shell structure that leads to two unsaturated bonds (radicals) in the defect junction, or (ii) a closed-shell structure leading to saturated bonds. However, after examining the DFT-calculated spin-density of finite ethynylene-anthracene monomer (see Figure 4e), it becomes clear that defect type B is associated with the closed-shell structure. In fact, both constant height STM image and dI/dV spectra acquired above the junction and adjacent anthracene monomer sites of a defect type B are featureless, similarly to that of defect at low energy (Figure 4f), pointing to the absence of extra charge localization at the junction.

Here two resonance forms can be considered for the close-shell structure regarding the conjugation of the adjacent linkers, leading to ethynylene or cumulene bridges (see Figure 4g). Two arguments suggest that the defect type B may adopt the cumulene-like structure. First, our nc-AFM images display lower

contrast and more elongated feature at the adjacent linkers compared to those at farther distances (cf Figure 4b). This intramolecular contrast is the result of the short-ranged Pauli repulsion being maximized in the areas of higher electron density so that minor variations in electron density assigned to specific bonding order can be resolved in nc-AFM images as features with different brightness or shape, thus pointing to an alternation in the character of the bond. On the other hand, such features can be further varied due to anisotropic charge distribution in the molecular backbone,<sup>[53]</sup> distinct interaction with the surface<sup>[54]</sup> and varying with the tip-sample distance. Second, Clar's aromatic  $\pi$ -sextet rule states that a resonance structure of polycyclic aromatic hydrocarbons with the maximal number of nonadjacent  $\pi$ -sextets represents the most stable form or the major resonance contributor. If we apply this rule in a local viewpoint in defect type B, we found that the cumulene transition increases the number of nonadjacent  $\pi$ -sextets from 2 (for the ethylene form) to 4 (cf Figure 4g).

Although a fully characterization of the mechanism behind the particular formation of such defects is beyond the scope of this article because it would involve complex quantum molecular mechanics calculations,<sup>[46,55]</sup> our findings suggest a mechanism to engineer low-dimensional defects in such polymers by placing an external source in UHV, which provides the system with atomic carbon atoms in a controllable manner during the polymerization reaction. In such a hypothetical experiment, one should expect to largely transform type B defects into type A.

## Conclusions

In conclusion, we report a strategy for thermally inducing low-dimensional structural defects that can imprint an open-shell character in on-surface synthesized  $\pi$ -conjugated polymers. High-resolution non-contact atomic force microscopy clarifies the structure of these defects, being those labeled type A and type B the most observed by far. We characterized the impact of these defects in the electronic properties of the polymer using a combination of scanning tunneling microscopy/spectroscopy experiments complemented with state-of-the-art density functional theory calculations. While the type B defect hardly affects the electronic structure of the polymer, the type A defect shows an intrinsic open-shell character which is of potential relevance for fundamental science, as well as in view of its potential applications, in materials chemistry and, particularly, in quantum electronic devices. The low bandgap of the polymer, and in particular, the proximity of the VB to the Fermi level, is a crucial aspect to stabilize the radical ground state of the type A defect. Our results show the growth and characterization of structural defects in  $\pi$ -conjugated polymers that address relevant electronic properties, thus contributing to the development of the field of on-surface chemistry and guiding the defect engineering of modern low-band-gap polymers.

## Methods

### Experimental Section

Experiments were performed in an ultra-high vacuum with a base pressure below  $5 \times 10^{-10}$  mbar system hosting a STM/nc-AFM (Createc GmbH) operated at 4.2 K. STM images were acquired in constant current mode with a bias voltage applied to the sample. For the spectroscopic measurements, specific site dI/dV were taken with the conventional lock-in technique with a modulation ranging from 0.5 mV to 10 mV at 937 Hz. STM/nc-AFM images were taken with sharpened by focus ion beam (FIB) Pt/Ir tips mounted on a qPlus sensor. In nc-AFM imaging, the tip was functionalized with a single CO molecule picked up from the bare metal substrate and operated in frequency-modulation mode (oscillated with a constant amplitude of 50 pm; resonant frequency  $\approx 30$  kHz; stiffness  $\approx 1800$  N/m). All nc-AFM images were acquired in constant height mode with a bias voltage of 1 mV. All images were subject to standard process using WSxM software.<sup>[56]</sup>

The Au(111) substrate was prepared by repeated cycles of Ar<sup>+</sup> sputtering (1 keV) and subsequent annealing. The molecular precursor was deposited by organic molecular beam epitaxy from a tantalum pocket maintained at 370 K onto a clean Au(111) held at room temperature. Whenever necessary samples were annealed to the desired temperature and subsequently transferred to the STM stage, which was kept at 4.2 K. For the temperature dependent STS data displayed in figures 3 g,h, the sample was heated up from 4.8 K by using a Zener diode mounted to the baseplate of the STM. The temperature was increased in a rate of 0.05–0.1 K / min. After reaching the temperature of interest, the system was thermalized for about 30–60 min.

Synthesis of molecular precursor 11,11,12,12-tetrabromoanthraquinodimethane is introduced elsewhere.<sup>[43]</sup>

## Theoretical Calculations

### Computational details

Density functional theory (DFT) calculations were performed using the FHI-AIMS code<sup>[57]</sup> within XC PBE0 functional<sup>[58,59]</sup> to describe the electronic properties of different gas-phase molecules. In all the calculations, we employed the light settings for the atomic basis sets. The atomic structures were relaxed until the total forces were smaller than  $10^{-2}$  eV Å<sup>-1</sup>. The relaxed structures were found by exploring different initial conditions and selecting the one with the lowest potential energy. Only the  $\Gamma$ -point was used for integration in the Brillouin zone.

### A. dI/dV simulations in the gas phase

Frontiers molecular orbitals were obtained from DFT calculations using the FHI-AIMS code within hybrid exchange-correlation functional PBE0<sup>[58,59]</sup> for the gas phase molecule. We employed Probe Particle Scanning Probe Microscopy (PP-SPM) code<sup>[59,60]</sup> to simulate constant-height dI/dV maps and CO-tip was represented by a linear combination of s-like (15 %) and px,py-like (85 %) orbitals without tip relaxation at tip-sample distance 5 Å.

### B. AFM Simulations

The AFM images were calculated using the probe particle model.<sup>[59]</sup> The parameters of the tip were chosen to mimic a CO-tip, using a quadrupole charge moment of  $-0.2$  e. Å<sup>2[58,61]</sup> and the lateral stiffness of the CO molecule is set to 0.25 N m<sup>-1</sup>. The electrostatic interaction was described in the AFM calculations using the potential calculated by DFT. To simulate the probe dynamics, we used typical values of a qPlus sensor, oscillation amplitude  $A = 100$  pm, sensor stiffness  $k = 3600$  N/m, and eigenfrequency  $f_0 = 30$  kHz.

## Author contributions

B.T. conceived and designed the experiments. D.E., P.J., and B.T. supervised the project and led the collaboration efforts. B.M., T.Ch., A.S.-G., B.C., and B.T. carried out the experiments and obtained the data. J.S. and N.M. synthesized the precursors. The experimental data were analyzed by B.M., D.E., P.J., and B.T., and discussed by all the authors. Q.Ch. and P.J. performed the theoretical calculations. The manuscript was written by B.M., D.E., P.J. and B.T., with contributions from all the authors.

## Acknowledgements

The authors gratefully acknowledge the support of the Operational Programme for Research, Development, and Education of

the European Regional Development Fund (Project No. CZ.02.1.01/0.0/0.0/16\_019/0000754). Q. Ch, B.M., and P.J. acknowledge the support of GACR 20–13692X. B.M. acknowledges the support from the Internal Student Grant Agency of the Palacký University in Olomouc, Czech Republic IGA\_PrF\_2021\_032 and the Fischer Scholarship. This project has received funding from Comunidad de Madrid [projects QUIMTRONIC-CM (Y2018/NMT-4783)], and Ministerio de Ciencia, Innovación y Universidades (projects PID2019-108532GB-I00). IMDEA Nanociencia is appreciative of support from the “Severo Ochoa” Programme for Centers of Excellence in R&D (MINECO, grant SEV-2016-0686).

## Conflict of Interest

The authors declare no conflict of interest.

## Data Availability Statement

The data that support the findings of this study are available from the corresponding author upon reasonable request.

**Keywords:** atomic force microscopy · conjugated polymers · on-surface synthesis · scanning tunneling microscopy

- [1] A. Kraft, A. C. Grimsdale, A. B. Holmes, *Angew. Chem. Int. Ed.* **1998**, *37*, 402–428; *Angew. Chem.* **1998**, *110*, 416–443.
- [2] Z. Qiu, B. A. G. Hammer, K. Müllen, *Prog. Polym. Sci.* **2020**, *100*, 101179.
- [3] J. Roncali, *Macromol. Rapid Commun.* **2007**, *28*, 1761–1775.
- [4] Y. Zhang, B. de Boer, P. W. M. Blom, *Phys. Rev. B: Condens. Matter Mater. Phys.* **2010**, *81*, 085201.
- [5] H. T. Nicolai, M. Kuik, G. A. H. Wetzelaer, B. de Boer, C. Campbell, C. Risko, J. L. Brédas, P. W. M. Blom, *Nat. Mater.* **2012**, *11*, 882–887.
- [6] D. Abbaszadeh, A. Kunz, N. B. Kotadiya, A. Mondal, D. Andrienko, J. J. Michels, G. J. A. H. Wetzelaer, P. W. M. Blom, *Chem. Mater.* **2019**, *31*, 6380–6386.
- [7] L. G. Kaake, P. F. Barbara, X. Y. Zhu, *J. Phys. Chem. Lett.* **2010**, *1*, 628–635.
- [8] R. Meng, Y. Li, C. Li, K. Gao, S. Yin, L. Wang, *Phys. Chem. Chem. Phys.* **2017**, *19*, 24971–24978.
- [9] L. Rومانer, A. Pogantsch, P. S. de Freitas, U. Scherf, M. Gaal, E. Zojer, E. J. W. List, *Adv. Funct. Mater.* **2003**, *13*, 597–601.
- [10] V. I. Arkhipov, P. Heremans, E. v. Emelianova, H. Bässler, *Phys. Rev. B* **2005**, *71*, 045214.
- [11] M. Silver, L. Pautmeier, H. Bässler, M. Silver, L. Pautmeier, H. Bässler, *SSCom* **1989**, *72*, 177–180.
- [12] V. I. Arkhipov, H. von Seggern, E. v. Emelianova, *Appl. Phys. Lett.* **2003**, *83*, 5074.
- [13] V. I. Arkhipov, E. v. Emelianova, G. J. Adriaenssens, *Phys. Rev. B* **2001**, *64*, 125125.
- [14] D. Hu, J. Yu, K. Wong, B. Bagchi, P. J. Rossky, P. F. Barbara, *Nature* **2000**, *405*, 1030–1033.
- [15] Z. Liang, A. Nardes, D. Wang, J. J. Berry, B. A. Gregg, *Chem. Mater.* **2009**, *21*, 4914–4919.
- [16] C. Tanase, P. W. M. Blom, D. M. de Leeuw, E. J. Meijer, *Phys. Status Solidi A* **2004**, *201*, 1236–1245.
- [17] L. Xu, J. Wang, J. W. P. Hsu, *Phys. Rev. Appl.* **2016**, *6*, 064020.
- [18] J. Yu, D. Hu, P. F. Barbara, *Science* **2000**, *289*, 1327–1330.
- [19] J. M. Lupton, P. Schouwink, P. E. Keivanidis, A. C. Grimsdale, K. Müllen, *Adv. Funct. Mater.* **2003**, *13*, 154–158.
- [20] P. A. Troshin, D. K. Susarova, Y. L. Moskvina, I. E. Kuznetsov, S. A. Ponomarenko, E. N. Myshkovskaya, K. A. Zakharcheva, A. A. Balakai, S. D. Babenko, V. F. Razumov, *Adv. Funct. Mater.* **2010**, *20*, 4351–4357.
- [21] L. Grill, S. Hecht, *Nat. Chem.* **2020**, *12*, 115–130.
- [22] Q. Shen, H. Y. Gao, H. Fuchs, *Nano Today* **2017**, *13*, 77–96.
- [23] S. Clair, D. G. de Oteyza, *Chem. Rev.* **2019**, *119*, 4717–4776.
- [24] J. Cai, P. Ruffieux, R. Jaafar, M. Bieri, T. Braun, S. Blankenburg, M. Muoth, A. P. Seitsonen, M. Saleh, X. Feng, K. Müllen, R. Fasel, *Nature* **2010**, *466*, 470–473.
- [25] G. Galeotti, F. de Marchi, E. Hamzehpoor, O. MacLean, M. Rajeswara Rao, Y. Chen, L. v. Besteiro, D. Dettmann, L. Ferrari, F. Frezza, P. M. Sheverdyayeva, R. Liu, A. K. Kundu, P. Moras, M. Ebrahimi, M. C. Gallagher, F. Rosei, D. F. Perepichka, G. Contini, *Nat. Mater.* **2020**, *19*, 874–880.
- [26] P. Ruffieux, S. Wang, B. Yang, C. Sanchez-Sanchez, J. Liu, T. Dienel, L. Talirz, P. Shinde, C. A. Pignedoli, D. Passerone, T. Dumsclaff, X. Feng, K. Müllen, R. Fasel, *Nature* **2016**, *531*, 489–492.
- [27] D. J. Rizzo, G. Veber, T. Cao, C. Bronner, T. Chen, F. Zhao, H. Rodriguez, S. G. Louie, M. F. Crommie, F. R. Fischer, *Nature* **2018**, *560*, 204–208.
- [28] O. Gröning, S. Wang, X. Yao, C. A. Pignedoli, G. Borin Barin, C. Daniels, A. Cupo, V. Meunier, X. Feng, A. Narita, K. Müllen, P. Ruffieux, R. Fasel, *Nature* **2018**, *560*, 209–213.
- [29] B. Cirera, A. Sánchez-Grande, B. de la Torre, J. Santos, S. Edalatmanesh, E. Rodríguez-Sánchez, K. Lauwaet, B. Mallada, R. Zbořil, R. Miranda, O. Gröning, P. Jelinek, N. Martín, D. Ećija, *Nat. Nanotechnol.* **2020**, *15*, 437–443.
- [30] A. Sánchez-Grande, J. I. Urgel, A. Cahlík, J. Santos, S. Edalatmanesh, E. Rodríguez-Sánchez, K. Lauwaet, P. Mutombo, D. Nachtigallová, R. Nieman, H. Lischka, B. de la Torre, R. Miranda, O. Gröning, N. Martín, P. Jelinek, D. Ećija, *Angew. Chem. Int. Ed.* **2020**, *59*, 17594–17599; *Angew. Chem.* **2020**, *132*, 17747–17752.
- [31] J. Lawrence, P. Brandimarte, A. Berdonces-Layunta, M. S. G. Mohammed, A. Grewal, C. C. Leon, D. Sánchez-Portal, D. G. de Oteyza, *ACS Nano* **2020**, *14*, 4499–4508.
- [32] L. Gross, F. Mohn, N. Moll, P. Liljeroth, G. Meyer, *Science* **2009**, *325*, 1110–1114.
- [33] L. Gross, B. Schuler, N. Pavliček, S. Fatayer, Z. Majzik, N. Moll, D. Peña, G. Meyer, *Angew. Chem. Int. Ed.* **2018**, *57*, 3888–3908; *Angew. Chem.* **2018**, *130*, 3950–3972.
- [34] D. G. de Oteyza, P. Gorman, Y. C. Chen, S. Wickenburg, A. Riss, D. J. Mowbray, G. Etkin, Z. Pedramrazi, H. Z. Tsai, A. Rubio, M. F. Crommie, F. R. Fischer, *Science* **2013**, *340*, 1434–1437.
- [35] A. Riss, A. P. Paz, S. Wickenburg, H. Z. Tsai, D. G. de Oteyza, A. J. Bradley, M. M. Ugeda, P. Gorman, H. S. Jung, M. F. Crommie, A. Rubio, F. R. Fischer, *Nat. Chem.* **2016**, *8*, 678–683.
- [36] A. Berdonces-Layunta, J. Lawrence, S. Edalatmanesh, J. Castro-Esteban, T. Wang, M. S. G. Mohammed, L. Colazzo, D. Peña, P. Jelinek, D. G. de Oteyza, *ACS Nano* **2021**, *15*, 5610–5617.
- [37] H. González-Herrero, J. I. Mendieta-Moreno, S. Edalatmanesh, J. Santos, N. Martín, D. Ećija, B. de la Torre, P. Jelinek, *Adv. Mater.* **2021**, *33*, 2104495.
- [38] J. Li, S. Sanz, M. Corso, D. J. Choi, D. Peña, T. Frederiksen, J. I. Pascual, *Nat. Commun.* **2019**, *10*, 200.
- [39] S. Mishra, D. Beyer, R. Berger, J. Liu, O. Gröning, J. I. Urgel, K. Müllen, P. Ruffieux, X. Feng, R. Fasel, *J. Am. Chem. Soc.* **2020**, *142*, 1147–1152.
- [40] Y. Zheng, C. Li, C. Xu, D. Beyer, X. Yue, Y. Zhao, G. Wang, D. Guan, Y. Li, H. Zheng, C. Liu, J. Liu, X. Wang, W. Luo, X. Feng, S. Wang, J. Jia, *Nat. Commun.* **2020**, *11*.
- [41] P. T. Landsberg in *Recombination in Semiconductors*, Cambridge University Press, Cambridge, **1991**.
- [42] R. Smith in *Semiconductors*, Cambridge University Press, Cambridge, **1959**.
- [43] A. Sánchez-Grande, B. de la Torre, J. Santos, B. Cirera, K. Lauwaet, T. Chutora, S. Edalatmanesh, P. Mutombo, J. Rosen, R. Zbořil, R. Miranda, J. Björk, P. Jelinek, N. Martín, D. Ećija, *Angew. Chem. Int. Ed.* **2019**, *58*, 6559–6563; *Angew. Chem.* **2019**, *131*, 6631–6635.
- [44] J. Kondo, *Prog. Theor. Phys.* **1964**, *32*, 37–49.
- [45] M. Ternes, A. J. Heinrich, W. D. Schneider, *J. Condens. Matter Phys.* **2008**, *21*, 053001.
- [46] B. de la Torre, A. Matěj, A. Sánchez-Grande, B. Cirera, B. Mallada, E. Rodríguez-Sánchez, J. Santos, J. I. Mendieta-Moreno, S. Edalatmanesh, K. Lauwaet, M. Otyepka, M. Medved, Á. Buendía, R. Miranda, N. Martín, P. Jelinek, D. Ećija, *Nat. Commun.* **2020**, *11*, 4567.
- [47] B. Schuler, S. Fatayer, F. Mohn, N. Moll, N. Pavliček, G. Meyer, D. Peña, L. Gross, *Nat. Chem.* **2016**, *8*, 220–224.
- [48] P. Zahl, Y. Zhang, *Energy Fuels* **2019**, *33*, 4775–4780.
- [49] H. O. Frota, *Phys. Rev. B* **1992**, *45*, 1096–1099.
- [50] O. Újsághy, J. Kroha, L. Szunyogh, A. Zawadowski, *Phys. Rev. Lett.* **2000**, *85*, 2557–2560.



- [51] Y. H. Zhang, S. Kahle, T. Herden, C. Stroh, M. Mayor, U. Schlickum, M. Ternes, P. Wahl, K. Kern, *Nat. Commun.* **2013**, *4*.
- [52] K. Nagaoka, T. Jamneala, M. Grobis, M. F. Crommie, *Phys. Rev. Lett.* **2002**, *88*.
- [53] B. Mallada, B. de la Torre, J. I. Mendieta-Moreno, D. Nachtigallova, A. Matěj, M. Matoušek, P. Mutombo, J. Brabec, L. Veis, T. Cadart, M. Kotora, P. Jelínek, *J. Am. Chem. Soc.* **2021**, *143*, 14694–14702.
- [54] S. Kawai, S. Nakatsuka, T. Hatakeyama, R. Pawlak, T. Meier, J. Tracey, E. Meyer, A. S. Foster, *Sci. Adv.* **2018**, *4*.
- [55] Y. Morita, S. Suzuki, K. Sato, T. Takui, *Nat. Chem.* **2011**, *3*, 197–204.
- [56] I. Horcas, R. Fernández, J. M. Gómez-Rodríguez, J. Colchero, J. Gómez-Herrero, A. M. Baro, *Rev. Sci. Instrum.* **2007**, *78*, 013705.
- [57] V. Blum, R. Gehrke, F. Hanke, P. Havu, V. Havu, X. Ren, K. Reuter, M. Scheffler, *Computer Comput. Phys. Commun.* **2009**, *180*, 2175–2196.
- [58] A. D. Becke, *Chem. Phys.* **1993**, *98*, 5648–5652.
- [59] P. Hapala, G. Kichin, C. Wagner, F. S. Tautz, R. Temirov, *P. Phys. Rev. B* **2014**, *90*, 085421.
- [60] O. Krejčí, P. Hapala, M. Ondráček, P. Jelínek, *Phys. Rev. B* **2017**, *95*.
- [61] J. Peng, J. Guo, P. Hapala, D. Cao, R. Ma, B. Cheng, L. Xu, M. Ondráček, P. Jelínek, E. Wang, Y. Jiang, *Nat. Commun.* **2018**, *9*.

---

Manuscript received: March 28, 2022

Accepted manuscript online: June 10, 2022

Version of record online: July 6, 2022